

The interaction of the halo around the butterfly planetary nebula NGC 650-1 with the interstellar medium

G. Ramos-Larios^{1*}, M.A. Guerrero², A. Nigoche-Netro¹, L. Olguín³, M.A. Gómez-Muñoz^{4,5}, L. Sabin⁶, R. Vázquez⁶, S. Akras⁷, J.C. Ramírez Vélez⁶ & M. Chávez⁸

¹Instituto de Astronomía y Meteorología, Dpto. Física, CUCEI, Universidad de Guadalajara, Av. Vallarta No. 2602, CP 44130, Guadalajara, Jalisco, Mexico

²Instituto de Astrofísica de Andalucía, IAA-CSIC, C/Glorieta de la Astronomía s/n, 18008 Granada, Spain

³Departamento de Investigación en Física, Universidad de Sonora, Blvd. Rosales-Colosio, Ed. 3H, 83190, Hermosillo, Sonora, Mexico

⁴Instituto de Astrofísica de Canarias, E-38200, La Laguna, Tenerife, Spain

⁵Departamento de Astrofísica, Universidad de La Laguna, E-38206, La Laguna, Tenerife, Spain

⁶Instituto de Astronomía, Universidad Nacional Autónoma de México, Apdo. Postal 877, 22860, Ensenada, B. C., Mexico

⁷Observatório Nacional/MCTI, Rua Gen. José Cristino, 77, 20921-400, Rio de Janeiro, Brazil

⁸Instituto Nacional de Astrofísica Óptica y Electrónica, Luis Enrique Erro No. 1, 72840, Tonantzintla, Puebla, Mexico

Received 2017 July 30th; in original form April 10th

ABSTRACT

With its bright and wide equatorial waist seen almost edge-on (“the butterfly body”) and the faint and broad bipolar extensions (“the butterfly wings”), NGC 650-1 is the archetypical example of bipolar planetary nebula (PN) with butterfly morphology. We present here deep high-resolution broad- and narrow-band optical images that expose the rich and intricate fine-structure of this bipolar PN, with small-scale bubble-like features and collimated outflows. A SHAPE spatio-kinematical model indicates that NGC 650-1 has a broad central torus with an inclination angle of 75° with respect to the line of sight, whereas that of the bipolar lobes, which are clearly seen in the position-velocity maps, is 85° . Large field of view deep images show, for first time, an arc-like diffuse envelope in low- and high-excitation emission lines located up to $180''$ towards the East-Southeast of the central star, well outside the main nebula. This morphological component is confirmed by *Spitzer* MIPS and *WISE* infrared imaging, as well as by long-slit low- and high-dispersion optical spectroscopic observations. *HST* images of NGC 650-1 obtained at two different epochs ~ 14 yrs apart reveal the proper motion of the central star along this direction. We propose that this motion of the star through the interstellar medium compresses the remnant material of a slow Asymptotic Giant Branch wind, producing this bow-shock-like feature.

Key words: (ISM planetary nebulae — ISM: jets and outflows — infrared: ISM — stars: AGB and post-AGB

1 INTRODUCTION

The morphology of planetary nebulae (PNe) is one of the most important issues in their study, displaying an enormous variety of shapes, sizes and complex structures. The Interacting Stellar Winds (ISW) (Kwok, Purton, & Fitzgerald 1978) and the Generalized Interacting Stellar Winds (GISW) models (Balick 1987) have made possible to explain the formation of the most general morphological classes of PNe by the interaction of the fast and tenuous stellar wind with the slow and dense Asymptotic Giant Branch (AGB) wind. The material ejected during the last phases of the AGB expands and disperses into the interstellar medium (ISM). It can still be seen as very weak and elusive haloes princi-

pally of round shape, but showing fanciful structures in occasions. Many authors have done great work concerning the search for halos in PNe, demonstrating in a certain way that halos are common in these objects (Chu, Jacoby, & Arendt 1987; Balick et al. 1992; Corradi et al. 2003).

Just recently, many serious amateur astronomers have obtained very deep images of PNe using modest aperture telescopes (Gabany & Martínez-Delgado 2011; Goldman 2013). By pushing the sensitivity of the observations using high-efficiency CCD cameras, dedicated narrow-band filters, and long exposure times, very low-surface brightness features not detected previously have been registered, resulting in findings of new structures.

This could be the case of NGC 650-1 ($\alpha=01^{\text{h}}42^{\text{m}}19.6^{\text{s}}$, $\delta=+51^\circ 34' 31.7$, J2000), a.k.a. the Little Dumbbell Nebula or M 76. Discovered in 1780 by P. Méchain and recorded the same year by

* E-mail: gerardo@astro.iam.udg.mx (GRL)

C. Messier, it was W. Herschel in 1787 who noticed that the nebula had two lobes barely separated, leading to the assignment of the two NGC numbers by J. Dreyer. The morphology of NGC 650-1 is reminiscent of a butterfly shape pattern, with a thick equatorial waist observed almost edge-on (“*the butterfly body*”) and two broad bipolar lobes (“*the butterfly wings*”). At a distance of only 0.93 ± 0.26 kpc (Frew, Parker, & Bojičić 2016), it is one of the most studied PNe. Previous works including optical images of NGC 650-1 exist (see, e.g. Balick et al. 1992; Corradi & Schwarz 1995; Hua 1997; Ramos-Larios, Phillips, & Cuesta 2008), but their resolution and depth are limited. The nebula has been described as a central elliptical ring seen nearly edge-on with two half-shells (Sabbadin & Hamzaoglu 1981). Its notorious axial symmetry and an inner rectangle with condensations was noted later (Recillas-Cruz & Pismis 1984), and then confirmed as a bipolar PN with a bright central ring with inner and outer lobes, the latter with a low expansion velocity of $\sim 5 \text{ km s}^{-1}$ (Bryce et al. 1996).

Using Hubble Space Telescope (*HST*) images and the spectral photometric characteristics of the central star, Koornneef & Pottasch (1998) were able to determine its temperature and V magnitude ($T_{\text{eff}} = 140,000 \text{ K}$, 17.48 mag., respectively) and determine a distance to NGC 650-1 of 1.2 kpc, similar to that of Felli & Perinotto (1979). The clumpy inner structure of the central bar, possibly produced by dust (Ramos-Larios, Phillips, & Cuesta 2008), suggests extinction variations. Radio emission at 6 cm is reported in this source, with the emission distributed mainly in the central and brightest regions of the core and lobes (Zijlstra, Pottasch, & Bignell 1989; Felli & Perinotto 1979). There is also further evidence for molecular emission. *Spitzer* mid-infrared (MIR) IRAC images (which probably contain molecular emission Hora et al. 2004) show that the emission at $8 \mu\text{m}$ extends over the shorter bands, whilst William Herschel Telescope (WHT) H_2 narrow-band imaging show knots and filaments of material in the core, mostly condensed at the tips of the major axis of the central ring but fainter and barely visible in the bipolar lobes (Marquez-Lugo et al. 2013). Akras, Gonçalves, & Ramos-Larios (2017) have recently presented the deepest H_2 images of PNe [H_2 (1-0) S1 and H_2 (2-1) S1] and proved that these small structures are also bright in low-ionization lines. In this context, it is interesting to highlight the MIR $8 \mu\text{m}$ emission found beyond the main ionized regions, which is due to Polycyclic Aromatic Hydrocarbon (PAH) band emission (Ramos-Larios, Phillips, & Cuesta 2008). It should be noted that CO molecular emission was not detected (Huggins & Healy 1989), although NGC 650-1 is a carbon-rich ($\text{C/O} > 2$) nebula (Kwitter & Henry 1996; van Hoof et al. 2013).

Photodetector Array Camera and Spectrometer (PACS) and Spectral and Photometric Imaging Receiver (SPIRE) images from the *Herschel* telescope found considerable extinction of ultraviolet (UV) photons inside the main torus of the nebula (Van de Steene et al. 2012). In this sense, an excellent work performed by van Hoof et al. (2013) with the same *Herschel* observations and using photoionization models found that the dust grains are large ($0.15 \mu\text{m}$) in the ionized main nebula, being heated both by stellar emission and diffuse $\text{Ly}\alpha$ emission from the ionized gas. They also derived a very high temperature of 208,000 K (50% higher than previously published values) for the central star.

The interaction between PNe and the surrounding ISM has been subject of various studies. Indeed, understanding this process will give us valuable clues about the local characteristics of the ISM as well as the chemistry, dynamics and kinematics of PNe. Hence, several objects showing a PN-ISM interaction have been discovered and studied (Borkowski, Sarazin, & Soker 1990;

Table 1. Optical Imaging

Telescope	Instrument	Filter	λ_c (Å)	$\Delta\lambda$ (Å)
IAC80	CAMELOT	[O III]	5007	30
		H α	6567	8
		[N II]	6571	50
NOT	ALFOSC	[O III]	5007	8
		H α	6567	8
		[N II]	6588	9
GTC	OSIRIS	g'	4815	1530
		r'	6410	1760
		OS657	6570	350

Tweedy & Kwitter 1996; Xilouris et al. 1996; Sabin et al. 2010). Most have been recently compiled and analyzed by Ali et al. (2012, 2013). The observations of these PNe clearly show different degrees or stages of interaction with the ISM, ranging from the sole interaction of the halo (remnant of a former AGB ejection or thermal pulse) surrounding the unaffected PN to the totally disrupted PN shell merging with the ISM. Wareing, Zijlstra, & O’Brien (2007) used hydrodynamical modelling and issued a classification (dubbed “WZO”) associated to the physical conditions of both the ISM and the PNe that declines into four stages of interaction WZO1–4. In particular, their WZO1 phase regroups all the objects in their early phase of interaction where the only affected component (in the form of a bow-shock) is the surrounding faint halo of the otherwise still morphologically intact PN. The number of PNe in the WZO1 stage represents $\sim 26\%$ of the whole sample of 117 objects compiled by Ali et al. (2012), based mainly on observations coming from Ramos-Larios & Phillips (2009) and Corradi et al. (2003). A cross check with the Hong Kong/AAO/Strasbourg H α PN database (HASH) (Parker et al. 2016) reveals 9 bipolar PNe with interacting halo: Cn 1-5, M 2-40, NGC 2440, NGC 3242, NGC 6765, NGC 6772, NGC 6804, NGC 6853, and NGC 7293. NGC 650-1 might add to this group.

With the purpose to investigating the real shape of this diffuse halo, their kinematics, composition and ISM interaction in NGC 650-1, we have used *Spitzer* MIPS and *WISE* infrared images, new deep and high-resolution broad- and narrow-band optical images, and long-slit low- and high-dispersion spectroscopic observations. These have been examined in conjunction with the SHAPE program (Steffen et al. 2011) in order to establish a simplified model of the whole PN.

The observations and archival data are presented in §2 and §3. The results on the morphology are described in §4. The spectroscopy is discussed in §5. The kinematics, model and the discussion are presented in §6 and final conclusions are presented in §7.

2 OPTICAL OBSERVATIONS

2.1 GTC imaging

A high-resolution broad-band colour composite image in the g' and r' Sloan filters and the Order Sorter (OS) OS657 filter was obtained from the Gran Telescopio Canarias (GTC) Astronomical Images Gallery (<http://www.gtc.iac.es/multimedia/imageGallery.php>). The series of images were acquired with the imager and spectro-

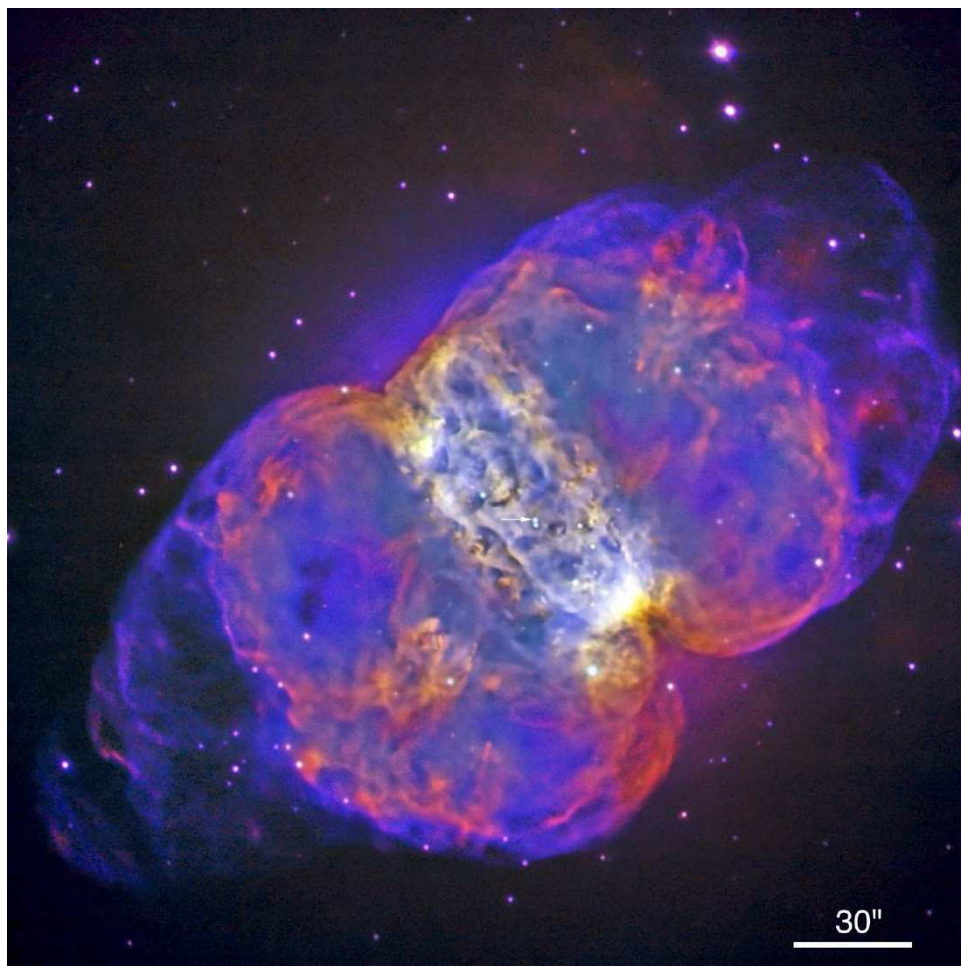


Figure 1. High-resolution colour hybrid composite combined picture of NGC 650-1 obtained through [O III] λ 5007 (blue), $H\alpha$ (green), and [N II] λ 6583 (red) narrow-band filters at the NOT, and g' (blue), r' (green) and OS657 (red) broad-band filters at the GTC (see text for details). In this picture, north is up, east to the left. This picture highlights the wealth of features in the main nebula associated with the bipolar lobes and equatorial ring. These show multiple clumps and filaments, mostly in emission, but also seen as dark absorptions projected onto the equatorial ring. The position of the central star is marked at the centre of the nebula by a small arrow. Note the hints of diffuse [O III] and [N II] barely visible just outside the nebular waist.

graph OSIRIS (Optical System for Imaging and low-Intermediate-Resolution Integrated Spectroscopy) at the Nasmyth-B focus of the GTC at the Observatorio del Roque de Los Muchachos (ORM), La Palma, Spain. The detector consists of a mosaic of two 2048×4096 Marconi CCD42-82 with pixel size of $15 \mu\text{m}$ and a binned 2×2 plate scale of $0''.254 \text{ arcsec pix}^{-1}$, resulting in a field of view (FoV) of $7'.8 \times 8'.5$ ($7'.8 \times 7'.8$ unvignetted). Three 30 s exposures were obtained in the g' and r' filters, and another three 60 s exposures were taken using the OS657 filter. The central wavelengths and bandwidths of all the optical observations filters are listed in Table 1.

2.2 NOT imaging

High-resolution [O III], $H\alpha$, and [N II] narrow-band images were obtained on September 3, 2008 using ALFOSC (Andalucia Faint Object Spectrograph and Camera) at the 2.56-m Nordic Optical Telescope (NOT) of the ORM. The detector was a 2048×2048 CCD with plate scale $0''.19 \text{ arcsec pix}^{-1}$, resulting in an FoV of $6'.5 \times 6'.5$. Two individual frames with integration times of 300 s were taken for each filter. All the data were bias-subtracted and flat-fielded using twilight flats employing standard IRAF routines. The spatial resolution, as derived from the full width half maximum

(FWHM) of stars in the FoV, was $\sim 0''.65$. A composite picture of the GTC and NOT combined images is shown in Figure 1.

2.3 IAC80 imaging

A very deep [O III], $H\alpha$, and [N II] narrow-band colour composite image was downloaded from the Banco de Imágenes Astronómicas (<http://www.bia.iac.es/>). The images were acquired on 2008 November 29, 2008 using the CAMELOT (CAmara MEjorada Liger del Observatorio del Teide) camera mounted at the 0.82-m IAC80 (Instituto de Astrofísica de Canarias) Telescope at the Observatorio del Teide in Tenerife, Spain.

A 2048×2048 CCD was used as detector. Its pixel size of $13.5 \mu\text{m}$ implies a plate scale of $0''.304 \text{ pixel}^{-1}$, resulting in an FoV of $10'.4 \times 10'.4$. Four frames with integration times of 1800 s each were taken for the $H\alpha$ and [N II] filters, and six frames with similar integration times were taken for the [O III] filter. All the data were processed using MAXIM DL¹ software. The seeing, as measured

¹ Suite of image acquisition, processing, and analysis tools by Cyanogen Imaging.

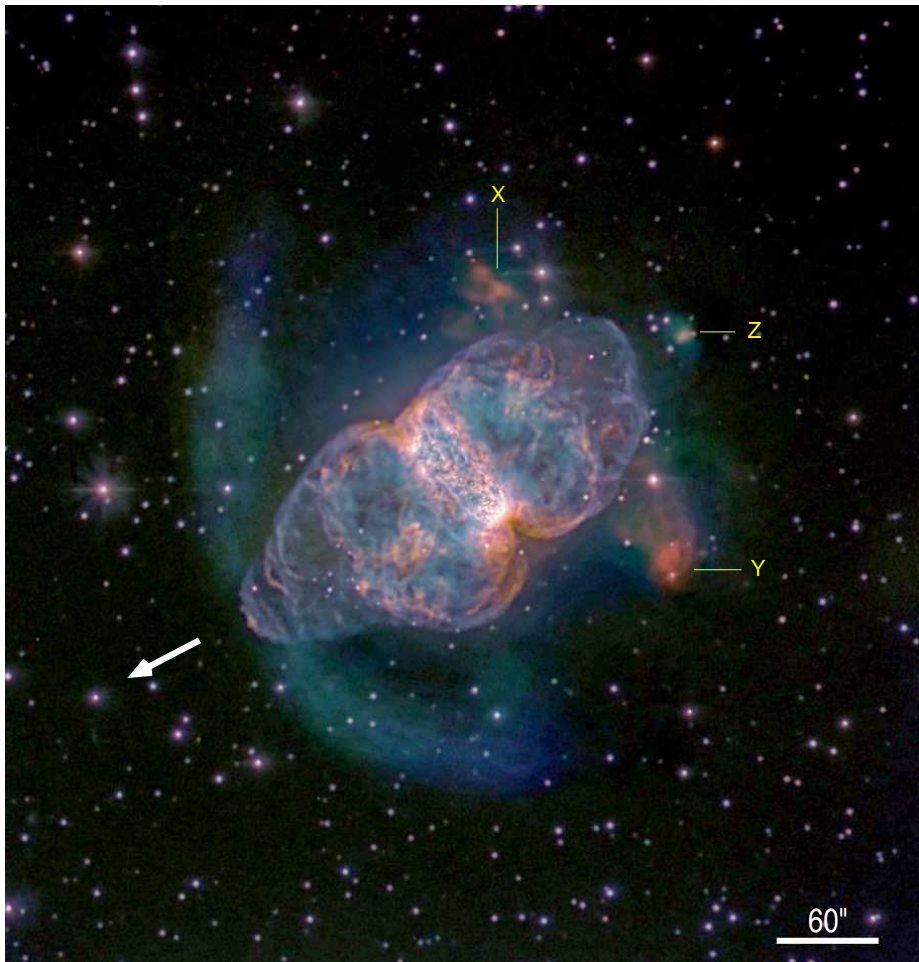


Figure 2. NOT and IAC80 [O III] $\lambda 5007$ (blue), H α (green), and [N II] $\lambda 6583$ (red) RGB hybrid composite combined picture of NGC 650-1. As in the image in Figure 1, north is up, east to the left. This combination improves the spatial resolution of the main nebula, and emphasizes the outer emission. Extended emission is clearly visible at distances up to $180''$ from the central star, with an arc-shaped feature of smooth diffuse H α and [O III] (green-blue) emissions pointing towards the East-South east, and [N II]-bright (red) patches and blobs (marked X,Y and Z) towards the West of the main nebula. The direction of the motion of the central star is marked with the big white arrow. The [N II] emission is mostly coincident with *Spitzer* MIR emission (Ramos-Larios, Phillips, & Cuesta 2008). Credit IAC80 image: Daniel López.

from stars in the FoV, was $\sim 0''.9$. A composite combined picture of the NOT and IAC80 images is shown in Figure 2.

2.4 Long-slit high-dispersion spectroscopy

Long-slit high dispersion optical spectroscopy of NGC 650-1 was obtained on October 21-22 2014 using the Manchester Echelle Spectrometer (MES, Meaburn et al. 2003) mounted on the 2.1 m (f/7.5) telescope at the Observatorio Astronómico Nacional de San Pedro Mártir (OAN-SPM, Mexico). A $2k \times 2k$ CCD with pixel size of $13.5 \mu \text{ pix}^{-1}$ was used as detector with a 2×2 on-chip binning, resulting on a plate scale of $0''.351 \text{ pix}^{-1}$. Since MES has no cross dispersion, a $\Delta\lambda = 90 \text{ \AA}$ bandwidth filter was used to isolate the 87th order covering the spectral range which includes the H α and [N II] $\lambda 6583$ lines, with a dispersion of $0.05 \text{ \AA pix}^{-1}$. The [O III] $\lambda 5007$ ($\Delta\lambda = 50$) filter was used to isolate the 114th order, corresponding to $0.043 \text{ \AA pix}^{-1}$. At this spectral orders, the slit width of $150\text{-}\mu\text{m}$ ($2''$) that was set during the observations corresponds to a spectral resolution of $\simeq 12 \text{ km s}^{-1}$.

Eight long-slit spectra, marked with the red labels S1 to S4 and S6 to S9 on the NOT-IAC80 greyscale image in the top panel

of Figure 3, were obtained to map the kinematics at different regions of the nebula. The position angles (PAs) for slits S1 to S4, measured in the conventional way anticlockwise from the north, are -3° , $+3^\circ$, $+110^\circ$, and $+120^\circ$, respectively, whilst for slits S6 to S9 are -49° , -55° , -36° , and 37° , respectively. The exposure time was 1,800 s for the spectra S1 to S4 and 1,200 s for the rest. The seeing during the observations, as determined from the FWHM of stars in the FoV, varied from $1''.2$ to $2''.0$. The spectra were wavelength calibrated with a ThAr arc lamp to an accuracy of $\pm 1 \text{ km s}^{-1}$ using IRAF.

2.5 Long-slit low-dispersion spectroscopy

A series of low dispersion, long-slit optical spectra of NGC 650-1 were obtained on October 27-28, 2014, using the Boller & Chivens (B&C) spectrometer mounted at the prime focus of the OAN-SPM 2.1m telescope. A 2048×2048 CCD was used as a detector, in conjunction with a $400 \text{ lines mm}^{-1}$ grating blazed at 5500 \AA . The slit had a length of $5'$ and a width of $200 \mu\text{m}$ ($\equiv 2''$). The plate and spectral scales were $0''.57 \text{ pixel}^{-1}$ and $1.7 \text{ \AA pixel}^{-1}$, respectively. The spectral resolution was $\sim 4 \text{ \AA}$, the wavelength uncertainty was ~ 1

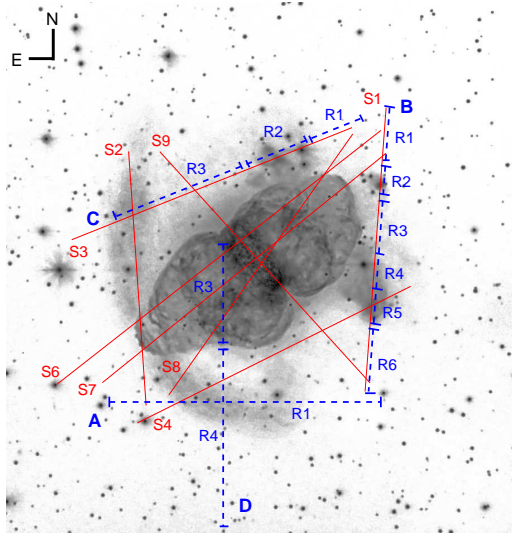


Figure 3. NOT-IAC80 (*top*), *Spitzer* MIPS 24 μm (*middle*), and *WISE* three-band colour composite (*bottom*) pictures of NGC 650-1. The NOT-IAC80 image has been labelled with the position of the long-slits used for the high- (solid red lines) and low-resolution (dashed blue lines) spectra. The regions used for the extraction of one-dimensional low-resolution spectra are marked on the four long-slits marked as A, B, C, and D.

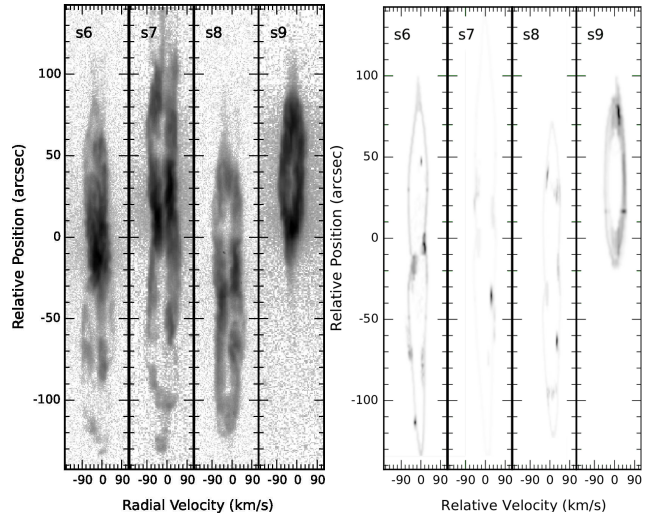


Figure 4. NGC 650-1 MES position-velocity (PV) map in the [O III] emission line (*left*) derived from the long-slits covering the main nebula (S6, S7, S8, and S9) and synthetic PV maps derived from our SHAPE model (*right*).

\AA , and the spectral range covered was 4080–7560 \AA . Three 1800 s exposure were obtained for every slit oriented through four main directions of PAs= 90, -4 , 110, and 0° named A, B, C and D respectively (marked in colour blue in the top panel of Figure 3). The mean air mass during the observations was $\simeq 1.1$. The observations were flux calibrated using a 300 s exposure of the star Hiltner 600 obtained on October 28. The seeing as determined from the FWHM of stars in the FoV, was $\simeq 2''$. The spectrum was bias-subtracted, flat-fielded, wavelength (CuAr lamp) and flux calibrated following standard procedures using XVISTA.

3 INFRARED DATA

3.1 WISE imaging

Wide-field Infrared Survey Explorer Space Telescope (*WISE*, Wright et al. 2010) observations of NGC 650-1 obtained in the W2, W3, and W4 bands were retrieved from the NASA/IPAC Infrared Science Archive (IRSA). *WISE* surveyed the entire sky at 3.4, 4.6, 12, and 22 μm (W1 to W4 bands) with angular resolutions of $6''$, $6''$, $6''$, and $12''$, respectively. The system consists of a 0.4m telescope using HgCdTe and Si:As 1024×1024 detector arrays with a plate scale of $2''$ 75 pixel^{-1} . Its astrometric accuracy for bright sources is better than $0''$ 15 . The *WISE* RGB composition image (bottom panel of Figure 3) where the W2 (blue), W3 (green) and W4 (red) bands were used, resembles the outer shape of the Figure 2, with the east-side of the nebulae showing a sharp boundary.

3.2 Spitzer MIPS images

Spitzer Space telescope Multiband Imaging Photometer for *Spitzer* (MIPS, Rieke et al. 2004) observations of NGC 650-1 were retrieved from the NASA/IPAC Infrared Science Archive (IRSA). NGC 650-1 was observed on September 2004 under the programme ID 77 (Stellar Ejecta: Macro-Molecule and Dust Formation and Evolution, PI: G. Rieke). MIPS produces image and photometry in three main bands, centred at 24 μm , 70 μm , and 160 μm , and low-resolution spectroscopic data in the range from 55 to 95 μm .

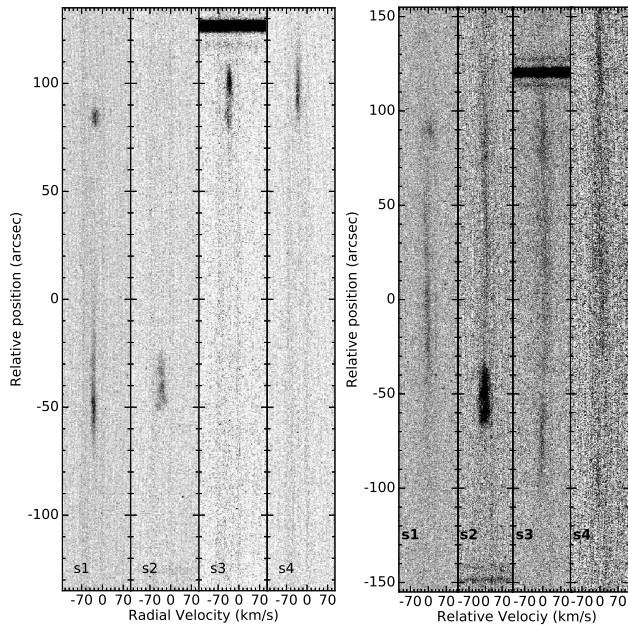


Figure 5. NGC 650-1 MES position-velocity (PV) maps in the [N II] (*left*) and [O III] (*right*) emission lines derived from the long-slits covering the halo (S1, S2, S3, and S4).

The MIPS detector consists of a Si:As 128×128 pixels array. The pixel size of $24 \mu\text{m}$ results in an FoV of $5'.4 \times 5'.4$. The MIPS observations were performed in the scan-mapping mode, used to image large areas of the sky in one or more bands simultaneously. The *Spitzer* $24 \mu\text{m}$ image (middle panel of Figure 3) shows the main nebula and the sharp edge of the outer structure towards the south-east.

4 MORPHOLOGY

The optical GTC, NOT, and IAC80 images and the archival IR *Spitzer* and *WISE* images have been presented in Figures 1, 2, and 3. The GTC and NOT unsharp masking colour **hybrid** composite picture in Figure 1 reveals fine details of the bipolar lobes and equatorial ring of NGC 650-1. The hybrid composite picture involves layering the higher resolution GTC image onto the lower resolution NOT image. In this case, this step enhances the small-scale structure features at the core region of NGC 650-1 seen in the GTC from the GTC image, whereas the more extended emission from the bipolar lobes present in the NOT image are emphasized. Meanwhile, the NOT and IAC80 unsharp masking colour **hybrid** composite picture in Figure 2 brings to life a new complex of low surface-brightness outer structures surrounding the main nebula. Here, the fainter large-scale structures are best imaged by the IAC80, with its larger pixel size and coarser spatial resolution, whereas the brighter emission from the main nebula is best resolved by the smaller pixel size and finer spatial resolution of the NOT images. Finally, the IR *Spitzer* and *WISE* images in Figure 3 complement the optical features with a view of the dusty outer component of NGC 650-1 and ionized main nebula as seen in IR emission lines. The different morphological components of NGC 650-1 are described next.

4.1 Main Nebula

The optical morphology of the main nebula is best seen in the NOT and GTC colour-composite picture presented in Figure 1. The main nebula consists of an equatorial ring and two broad bipolar lobes with prominent polar protrusions. The bipolar morphology of NGC 650-1, which is very similar to that of other butterfly-shaped PNe such as Sh 1-89 (Manchado et al. 1996), has been described many times in the literature (e.g. Balick 1987; Sabin et al. 2012; Guerrero et al. 2013; Uscanga et al. 2014; Manchado et al. 2015). In this section we will focus on the new details revealed by the NOT and GTC images.

The equatorial ring has a size $\sim 95''$ and is oriented along PA $\sim 35^\circ$. There is a notable ionization gradient, with the [N II] emission distributed mostly along the outer edges of the ring, the [O III] emission mostly on the central regions, and the $H\alpha$ emission delineating the ring at intermediate radial distances from the central star. The ring interior is filled with emission that follows an intricate pattern of filaments and patches, but it also reveals dark filaments and blobs that absorb the emission in the background. These higher density regions may be associated with the molecular-rich filaments and knots with bright H_2 emission (Marquez-Lugo et al. 2013; Manchado et al. 2015).

Diffuse [O III] and [N II] emission is faintly visible towards the North and South of the nebular waist, respectively. A few arc-like features are hinted in the southern region, although these smooth features are not as clear as those detected in IC 4406 (Ramos-Larios et al. 2016) and NGC 2346 (Phillips & Ramos-Larios 2010), where it has been presumed the possible existence of ring-like structures associated with the detailed mass-loss in the last phases of the AGB (Corradi et al. 2004; Kim et al. 2017).

Two broad bipolar lobes protrude from the equatorial ring. The bipolar lobes are especially prominent in [N II], with emission concentrated along the outer edges of the bipolar lobes (red in Figures 1 and 2). The [N II] emission seen inside the bipolar lobes most likely corresponds to regions of bright [N II] emission at the walls of the bipolar lobes projected inside them. There are many interesting features, such as radial filaments (in red in Figure 1) pointing towards the central star and dark patches indicating the presence of foreground absorbing material.

The broad butterfly-shaped bipolar lobes show extensions at their tips, with a single bow-shock feature towards the Southeast and several (at least three) similar structures towards the Northwest. The emission from these structures is mostly dominated by [O III], may be revealing a higher excitation caused by illumination effects or by shocks (Guerrero et al. 2000).

4.2 Extended Outer Emission

The optical morphology of the extended outer emission is best seen in the NOT and IAC80 colour-composite picture presented in Figure 2. The outer emission consists of an arc-like feature located towards the East-Southeast of the main nebula and [N II] blobs above and below the western bipolar lobe of NGC 650-1.

The arc-shaped feature presents smooth diffuse $H\alpha$ and [O III] (green-blue in Figure 2) emissions. This arc-like feature is symmetric with respect to the bipolar axis of the main nebula, with the $H\alpha$ emission dominating the central regions of the arc and the [O III] emission been more intense at its outer edges. Interestingly, if we drew two lines connecting the edges of this arc-like feature with the central star, these lines will touch the tips of the equatorial ring,

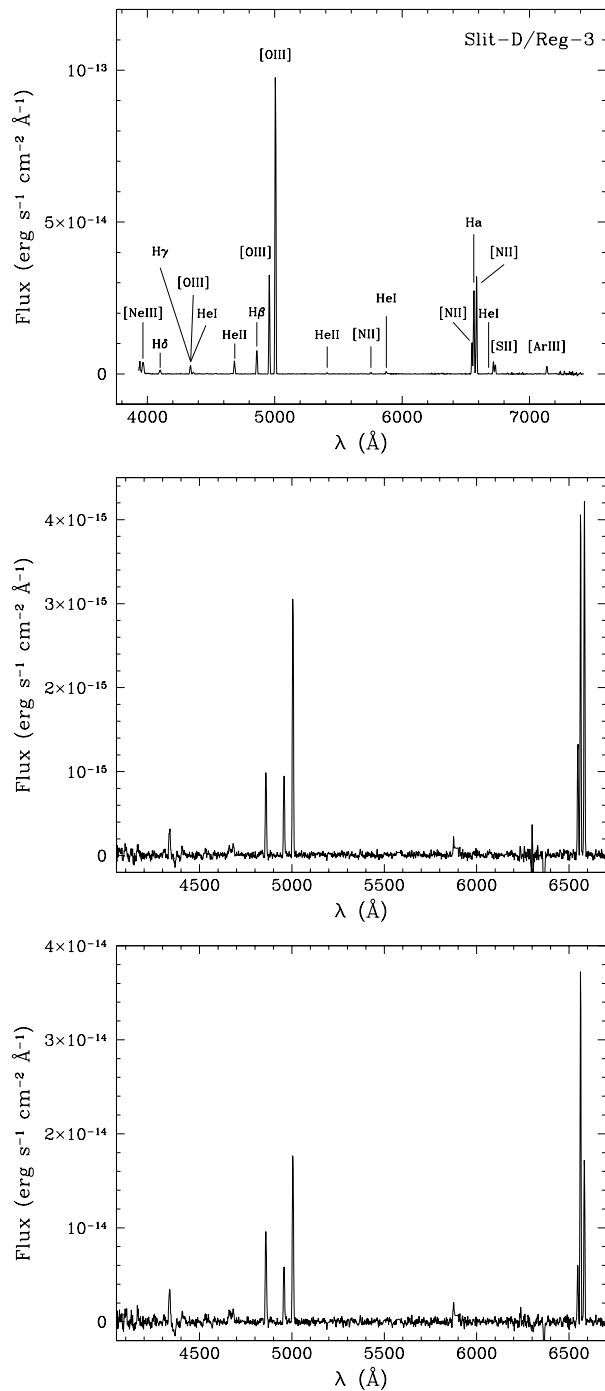


Figure 6. From top to bottom, SPM B&C low-dispersion long-slit optical spectra of NGC 650-1 for the eastern bipolar lobe (region 3 of slit D) and regions of low- (*middle*) and high-excitation (*bottom*) in the halo (see text for details). The main spectral lines are identified on the top spectrum.

thus suggesting the arc-like feature may result from illumination effects (Kwok 2010). The centre of this arc-like feature, if we assume it is an arc of a circle, would be located $\sim 60''$ west-northwest of the central star. The radius of such circle would be $220''$.

As for the [N II]-bright western blobs, these are two disconnected patches of low-excitation diffuse emission located below and above the western bipolar lobe along a line orthogonal to the bipolar axis (labelled X and Y in Figure 2). The southern blob “Y”

is brighter and more extended than the northern blob “X”. There is another [N II]-bright knot just at the tip of the western bipolar lobe (labelled Z in Figure 2), but it seems the tip of a bipolar protrusion which is only faintly detected.

4.3 IR imaging

Near- and mid-IR studies of NGC 650-1 abound in the literature. Ueta (2006) has analysed the $24\ \mu\text{m}$, $70\ \mu\text{m}$, and $160\ \mu\text{m}$ *Spitzer* MIPS observations of NGC 650-1, focusing on the main nebula. The bipolar lobes (and its protrusions) and the equatorial ring of NGC 650-1 are clearly revealed, indeed, in the $24\ \mu\text{m}$ image presented in the middle panel of Figure 3. Ueta (2006) remarked that the emission from the equatorial ring in the $24\ \mu\text{m}$ image actually peaks inside the edges of the emission from ionized material. The spatial coincidence of the $24\ \mu\text{m}$ emission with that of the He II emission reported by Balick (1987) indicates that the emission at this location in this band is dominated by the [Ne V] $24.3\ \mu\text{m}$ and [O IV] $25.9\ \mu\text{m}$ emission lines (van Hoof et al. 2013; Clayton et al. 2014).

Otherwise, the $24\ \mu\text{m}$ *Spitzer* MIPS image discloses an arc of diffuse emission towards the East-Southeast which is coincident with the arc-like feature seen in the optical H α and [O III] emission lines. This same structure is traced by the *WISE* W4 band image (red colour in the bottom panel of Figure 3).

5 SPECTROSCOPY

As previously shown, the deep IAC80 image has revealed an interesting outer structure around the butterfly-shaped main nebular shell of NGC 650-1. To investigate its nature, we have obtained low- and high-dispersion long-slit spectra at selected positions to obtain information on its excitation conditions and kinematics.

The high-dispersion echelle data probe both the bipolar main nebula and the outer structure. The kinematics of the main bipolar nebula has been thoroughly discussed in the literature (Taylor 1979; Sabbadin & Hamzaoglu 1981; Recillas-Cruz & Pismis 1984; Bryce et al. 1996). Our long-slit echelle spectra (Figure 4) and the resulting SHAPE modelling are consistent with the distinguished work presented by Bryce et al. (1996). The main nebula can be described as a thick equatorial ring that collimates two broad bipolar lobes. The inclination of the bipolar axis with the line of sight is $\sim 85^\circ$, with the eastern lobe receding from us. The de-projected velocity of the bipolar lobes range between 120 and $140\ \text{km s}^{-1}$, whilst that of the equatorial ring is $\sim 37\ \text{km s}^{-1}$. At a distance of $0.93\ \text{kpc}$, the kinematical age is $\simeq 4760\ \text{yrs}$. The nebula has a systemic LSR velocity of $-22\ \text{km s}^{-1}$ as derived from the average radial velocity of the equatorial ring. Unless stated otherwise, the radial velocities of the different features of NGC 650-1 will be referred to this systemic velocity.

The features in the outermost regions have rather small velocities (Figure 5). The eastern bow-shock has a velocity of $-2\ \text{km s}^{-1}$ and the material behind it $-3\ \text{km s}^{-1}$ (northern region registered by slit #3) and $\sim 0\ \text{km s}^{-1}$ (western region registered by slit #1). The [N II]-bright blobs have relatively larger velocities, in the range of $-10\ \text{km s}^{-1}$.

One-dimensional low-dispersion spectra from 7 different regions have been extracted to probe the bow-shock structure and regions immediately behind it. As marked in the top panel of Figure 3, these are the apertures #1 of slit A, #1, #3, and #6 of slit B, #1 and #3 of slit C, and #4 of slit D. Similarly, four one-dimensional

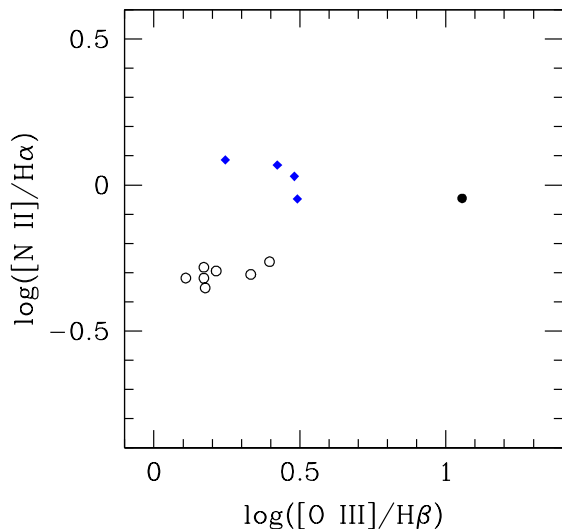


Figure 7. Line intensity ratios derived from low-dispersion long-slit optical spectra of the bipolar lobes of NGC 650-1 (black solid dots), the outer [N II]-bright blobs (blue solid diamonds), and the outer arc-like features (black open circles).

low-dispersion spectra have been extracted to probe the [N II]-bright blobs, namely apertures #2, #4, and #5 of slit B, and #2 of slit C.

Once we have confirmed that the spectra of each morphological component share the same spectral properties, we have combined them to increase their S/N ratio. The combined spectra are presented in Figure 6, corresponding to the [N II]-bright blobs (middle panel) and to the bow-shock structure and regions immediately behind it (bottom panel).

The $H\alpha$ surface brightness of these two regions is $\cong 1 \times 10^{-17}$ and $\cong 4 \times 10^{-17}$ erg cm s^{-1} arcsec $^{-2}$, respectively.

To compare their spectral properties with those of the main nebula, one additional spectrum probing the eastern bipolar lobe has been extracted from the aperture #3 of slit D. This spectrum is presented at the top panel of Figure 6.

We have measured the intensities of the $H\beta$, $H\alpha$, [O III] $\lambda 5007$, and [N II] $\lambda 6584$ in these spectra. Their ratios are shown in Figure 7. The low-dispersion spectroscopic data confirm the excitation variations through the different components of the outer emission seen in the IAC80 image (Figure 2). The [N II]-bright blobs have [N II]/ $H\alpha$ similar to those of the bipolar lobes, but much lower [O III]/ $H\beta$, thus implying significantly higher [N II]/[O III], typical for low-ionization structures in PNe (Akras & Gonçalves 2016). Meanwhile, the bow-shock structure has both lower [N II]/ $H\alpha$ and [O III]/ $H\beta$ line ratios than the bipolar lobes, revealing the relative prevalence of the recombination lines over the collisionally excited lines in this region.

6 DISCUSSION

The spatio-kinematical analysis presented in the previous sections implies two different structural components in NGC 650-1: the well-known bipolar main nebula and a previously unreported outer structure consisting of an arc of smooth emission and several low-excitation blobs. We describe next these two structural components.

6.1 The Main Nebula of NGC 650-1

The spatio-kinematical model of the main nebula of NGC 650-1 presented in §5 is very similar to that presented by Bryce et al. (1996). The equatorial region can be described as a thick ring from which two bipolar lobes protrude. These bipolar lobes show notable extensions at their tips. The inclination angle of the equatorial ring and bipolar lobes, in the range between 75° and 85° , places the nebula symmetry axis close to the plane of the sky.

The bipolar lobes of NGC 650-1 have been described profusely in the literature (Sabbadin & Hamzaoglu 1981; Recillas-Cruz & Pismis 1984; Bryce et al. 1996; Ueta 2006) and they will not be discussed here. As for the equatorial ring, the new images reveal a wealth of complexity.

There is a significant ionization structure, with the He II and [Ne V] emissions inside the ring, and the [N II] emission delineating its outer edge. This betrays the high temperature of its central star, which has been estimated to be 208,000 K (van Hoof et al. 2013). It is thus perplexing that this high-excitation gas inside the equatorial ring coexists with dust and H_2 molecular material as revealed by the presence of dark knots and filaments in the optical images and clumpy H_2 emission in near-IR images.

This suggests that high density clumps and filaments still withstand the action of the stellar wind and high ionization stellar flux, although the alignment along the line of sight of different gas phases at the ionization front cannot be neglected (Ueta 2006).

6.2 The Halo around NGC 650-1

The deep IAC80 image of NGC 650-1 has revealed a new set of features beyond the extent of the main nebula (Figure 2). This can be classified as a halo ejected during the AGB phase (Chu, Jacoby, & Arendt 1987; Stanghellini & Pasquali 1995). The leading edge of the halo, with its bow-shock morphology, is clearly seen in the *Spitzer* MIPS $24\mu m$ image, but it is undetected in the $70\mu m$ and $160\mu m$ MIPS images (Ueta 2006). It is well detected in the *WISE* W4 band (red colour in the bottom panel of Figure 3). Although the emission in the *Spitzer* MIPS $24\mu m$ band of the equatorial ring of NGC 650-1 was attributed to the [O IV] 25.9μ and [Ne V] $24.3\mu m$ line emission, the origin of this emission in this region of the halo may be different. This band also includes dust continuum emission (Chu et al. 2009), which is very likely dominant in this region, given its distance to the ionizing source. This would be consistent with the lower excitation of this region revealed by the optical spectra.

The overall morphology of the halo is very reminiscent of that resulting from the interaction of a low density nebula with the ISM (Villaver, Manchado, & García-Segura 2012; Wareing, Zijlstra, & O’Brien 2007). Therefore, we propose that the outer emission of NGC 650-1 corresponds to a halo ejected during the AGB phase which is interacting with the ISM. As the star moves through the ISM, the leading edge of the halo is compressed, forming the eastern arc-like feature (a bow-shock). Meanwhile, material stripped from the halo in its interaction with the ISM is seen in the trailing side as blobs and clumps particularly bright in the low-excitation line of [N II]. The density of these clumps is low, however, as revealed by their low $H\alpha$ surface brightness.

This conclusion is supported by its kinematic properties. The radial velocity of the different features of the halo registered by our long-slit echelle spectroscopy shows small differences, in the range between 3 and 10 km s^{-1} , with the systemic velocity of the nebula. In all cases, the velocity of the halo are blue-shifted with respect

to the nebula systemic velocity, indicating that the halo approaches us, i.e., it is placed between the nebula and us. If we adopt an expansion velocity of 10 km s^{-1} , then at the distance of 0.93 kpc, the kinematical age of this halo would be $\sim 80,000 \text{ yrs}^2$.

Naively, the halo bow-shock structure would be expected to be oriented along the direction of the relative motion of the central star of NGC 650-1 and the local ISM. Under this assumption, the fact that the bow-shock shares its symmetry axis with the bipolar axis of the main nebula of NGC 650-1 should be coincidental, although illumination effects cannot be neglected: we might just see the section of the leading halo which is illuminated by the central star, resulting in the apparent alignment between the bow-shock at the halo and the bipolar symmetry axis. On the other hand, the protrusions emanating from the eastern lobe are indicative of compression, which is further supported by its rippled morphology. This is not the case for the much weaker protrusions emanating from the western lobe.

To determine the motion of the central star of NGC 650-1 on the plane of the sky, we have used two *HST* images obtained in 1995.59 and 2009.75 (i.e., 14.16 years apart) to derive a proper motion of $0''.0075 \text{ yr}^{-1}$ along $\text{PA} \simeq 112^\circ$. At the distance of 0.93 kpc, this proper motion implies a velocity of $\sim 34 \text{ km s}^{-1}$ on the plane of the sky. The nebula moves almost parallel to the Galactic Plane, at a height below it of $\sim 170 \text{ pc}$.

The systemic velocity of the nebula is -22 km s^{-1} , which we will adopt as the radial velocity of its central star. The motion of the central star along the line of sight, approaching us, is consistent with the blue-shifted halo. More importantly, the motion of the central star on the plane of the sky along $\text{PA} \simeq 112^\circ$ is in great agreement with the symmetry axis of the bipolar main nebula at 125° . It can be concluded that the nebula as a whole, main nebula and halo, moves towards the East-Southeast direction, compressing the eastern section of the halo into a bow-shock feature and the protrusions from the eastern bipolar lobe. The trailing material of the halo is seen as the [N II]-bright blobs.

7 SUMMARY

We report for the first time the discovery of a halo around the butterfly PN NGC 650-1. This demonstrates that the quotation from Balick's paper "This is an outstanding example of an object for which a short exposure tells a very different story from a long one" (Balick et al. 1992) perfectly applies. Indeed, they did not detect this halo, but proposed the confinement of the main nebula by an "invisible low-density medium" as suggested by the absence of ionization fronts and the sharp edges of the lobes. Our work confirms the validity of their conclusions, implying that the "invisible low-density medium" is real.

It is worthwhile to ask oneself whether all bipolar PNe have spherical haloes. Some of them have already been reported in the literature, as the ones around Vy 1-2 (Akraş et al. 2015; Ramos-Larios et al. 2016) and NGC 6905 (Rubio et al. 2015). Many other may wait for detection, but they may be very faint (as the one detected here in NGC 650-1) or they might have been

stripped by the interaction with the ISM. New deep sensitive images are required for many objects with similar characteristics.

ACKNOWLEDGMENTS

GRL acknowledges support from Universidad de Guadalajara (Apoyo de Estancias Académicas – RG/003/2017), CONACyT, CGCI, PRODEP and SEP (Mexico). MAG also acknowledges support of the grant AYA 2011-29754-C03-02 and AYA 2014-57280-P, both co-funded with FEDER funds. LS acknowledges support from PAPIIT grant IA-101316.

Based on observations made with the Observatorio Astronómico Nacional at the Sierra de San Pedro Mártir, OAN-SPM, which is operated by the Instituto de Astronomía of the Universidad Nacional Autónoma de México. Based on observations made with the Nordic Optical Telescope, operated on the island of La Palma jointly by Denmark, Finland, Iceland, Norway, and Sweden, in the Spanish Observatorio del Roque de Los Muchachos of the Instituto de Astrofísica de Canarias. The data presented here were obtained [in part] with ALFOSC, which is provided by the Instituto de Astrofísica de Andalucía (IAA) under a joint agreement with the University of Copenhagen and NOTSA. This article is based on observations made with the IAC80 operated on the island of Tenerife by the IAC in the Spanish Observatorio del Teide. Based on observations made with the Gran Telescopio Canarias (GTC), installed in the Spanish Observatorio del Roque de los Muchachos of the Instituto de Astrofísica de Canarias, in the island of La Palma. This publication makes use of data products from the Wide-field Infrared Survey Explorer, which is a joint project of the University of California, Los Angeles, and the Jet Propulsion Laboratory/California Institute of Technology, funded by the National Aeronautics and Space Administration. This work is based [in part] on observations made with the Spitzer Space Telescope, which is operated by the Jet Propulsion Laboratory, California Institute of Technology under a contract with NASA. IRAF, the Image Reduction and Analysis Facility, is distributed by the National Optical Astronomy Observatory, which is operated by the Association of Universities for Research in Astronomy (AURA) under cooperative agreement with the National Science Foundation. XVIDA is an interactive image and spectral reduction and analysis package developed at the Lick Observatory and maintained and distributed by Jon Holtzman at the New Mexico State University at <http://ganymede.nmsu.edu/holtz/xvista/>.

REFERENCES

- Akraş S., Boumis P., Meaburn J., Alikakos J., López J. A., Gonçalves D. R., 2015, MNRAS, 452, 2911
- Akraş S., Gonçalves D. R., 2016, MNRAS, 455, 930
- Akraş S., Gonçalves D. R., Ramos-Larios G., 2017, MNRAS, 465, 1289
- Ali A., Sabin L., Snaid S., Basurah H. M., 2012, A&A, 541, A98
- Ali, A., Ismail, H. A., Snaid, S., & Sabin, L. 2013, A&A, 558, A93
- Balick B., 1987, AJ, 94, 671
- Balick B., Gonzalez G., Frank A., Jacoby G., 1992, ApJ, 392, 582
- Borkowski K. J., Sarazin C. L., Soker N., 1990, ApJ, 360, 173
- Bryce M., Mellema G., Clayton C. A., Meaburn J., Balick B., López J. A., 1996, A&A, 307, 253
- Chu Y.-H., Jacoby G. H., Arendt R., 1987, ApJS, 64, 529

² We note the strong dynamical interaction of this halo with the ISM, which will affect both its radius and expansion velocity. Villaver, Manchado, & García-Segura (2002) have modelled this interaction and concluded that kinematic ages derived for PN haloes are unreliable. The kinematic age provided here for the halo of NGC 650-1 should be used as a first order estimate of its age.

- Chu Y.-H., et al., 2009, *AJ*, 138, 691
- Clayton G. C., De Marco O., Nordhaus J., Green J., Rauch T., Werner K., Chu Y.-H., 2014, *AJ*, 147, 142
- Corradi R. L. M., Schwarz H. E., 1995, *A&A*, 293, 871
- Corradi R. L. M., Schönberner D., Steffen M., Perinotto M., 2003, *MNRAS*, 340, 417
- Corradi R. L. M., Sánchez-Blázquez P., Mellema G., Gianmanco C., Schwarz H. E., 2004, *A&A*, 417, 637
- Felli M., Perinotto M., 1979, *A&A*, 76, 69
- Frew D. J., Parker Q. A., Bojičić I. S., 2016, *MNRAS*, 455, 1459
- Gabany R. J., Martínez-Delgado D., 2011, *SASS*, 30, 1; Editors: Brian D. Warner, Jerry Foote and Robert Buchheim, Published by the Society for Astronomical Sciences, Inc., Big Bear Lake, CA
- Goldman D. S., 2013, *Narrowband Imaging*. In: Gendler R. (eds) *Lessons from the Masters. The Patrick Moore Practical Astronomy Series*, vol 179. Springer, New York, NY
- Guerrero M. A., Villaver E., Manchado A., Garcia-Lario P., Prada F., 2000, *ApJS*, 127, 125
- Guerrero M. A., Miranda L. F., Ramos-Larios G., Vázquez R., 2013, *A&A*, 551, A53
- Hora J. L., Latter W. B., Allen L. E., Marengo M., Deutsch L. K., Pipher J. L., 2004, *ApJS*, 154, 296
- Hua C. T., 1997, *A&AS*, 125,
- Huggins P. J., Healy A. P., 1989, *ApJ*, 346, 201
- Kim H., Trejo A., Liu S.-Y., Sahai R., Taam R. E., Morris M. R., Hirano N., Hsieh I.-T., 2017, *NatAs*, 1, 0060
- Koornneef J., Pottasch S. R., 1998, *A&A*, 335, 277
- Kwitter K. B., Henry R. B. C., 1996, *ApJ*, 473, 304
- Kwok S., Purton C. R., Fitzgerald P. M., 1978, *ApJ*, 219, L125
- Kwok S., 2010, *PASA*, 27, 174
- Levi L., 1974, *Comput. Graphics Image Processing*, 3, 163
- Manchado A., Guerrero M. A., Stanghellini L., Serra-Ricart M., 1996, *The IAC morphological catalog of northern Galactic planetary nebulae*. Instituto de Astrofísica de Canarias (IAC), La Laguna, Spain
- Manchado A., Stanghellini L., Villaver E., García-Segura G., Shaw R. A., García-Hernández D. A., 2015, *ApJ*, 808, 115
- Marquez-Lugo R. A., Ramos-Larios G., Guerrero M. A., Vázquez R., 2013, *MNRAS*, 429, 973
- Meaburn J., López J. A., Gutiérrez L., Quiróz F., Murillo J. M., Valdéz J., Pedrayez M., 2003, *RMxAA*, 39, 185
- Parker, Q. A., Bojičić, I. S., & Frew, D. J. 2016, *Journal of Physics Conference Series*, 728, 032008
- Phillips J. P., Ramos-Larios G., 2010, *MNRAS*, 405, 2179
- Ramos-Larios G., Phillips J. P., Cuesta L., 2008, *MNRAS*, 391, 52
- Ramos-Larios G., Phillips J. P., 2009, *MNRAS*, 400, 575
- Ramos-Larios G., Santamaría E., Guerrero M. A., Marquez-Lugo R. A., Sabin L., Toalá J. A., 2016, *MNRAS*, 462, 610
- Recillas-Cruz E., Pismis P., 1984, *MNRAS*, 210, 57
- Rieke G. H., et al., 2004, *ApJS*, 154, 25
- Rubio G., Vázquez R., Ramos-Larios G., Guerrero M. A., Olguín L., Guillén P. F., Mata H., 2015, *MNRAS*, 446, 1931
- Sabbadin F., Hamzaoglu E., 1981, *MNRAS*, 197, 363
- Sabin L., Zijlstra A. A., Wareing C., Corradi R. L. M., Mampaso A., Viironen K., Wright N. J., Parker Q. A., 2010, *PASA*, 27, 166
- Sabin L., Vázquez R., López J. A., García-Díaz M. T., Ramos-Larios G., 2012, *RMxAA*, 48, 165
- Stanghellini L., Pasquali A., 1995, *ApJ*, 452, 286
- Steffen, W., Koning, N., Wenger, S., Morisset, C., & Magnor, M. 2011, *IEEE Transactions on Visualization and Computer Graphics*, 17, 454
- Taylor K., 1979, *MNRAS*, 189, 511
- Tweedy R. W., Kwitter K. B., 1996, *ApJS*, 107, 255
- Ueta T., 2006, *ApJ*, 650, 228
- Uscanga L., Velázquez P. F., Esquivel A., Raga A. C., Boumis P., Cantó J., 2014, *MNRAS*, 442, 3162
- Van de Steene G. C., Exter K. M., van Hoof P. A. M., Lim T. L., Barlow M. J., Matsuura M., Ueta T., 2012, *IAUS*, 283, 514
- van Hoof P. A. M., et al., 2013, *A&A*, 560, A7
- Villaver E., Manchado A., García-Segura G., 2002, *ApJ*, 581, 1204
- Villaver E., Manchado A., García-Segura G., 2012, *ApJ*, 748, 94
- Wareing C. J., Zijlstra A. A., O'Brien T. J., 2007, *MNRAS*, 382, 1233
- Wright E. L., et al., 2010, *AJ*, 140, 1868
- Xilouris, K. M., Papamastorakis, J., Paleologou, E., & Terzian, Y. 1996, *A&A*, 310, 603
- Zijlstra A. A., Pottasch S. R., Bignell C., 1989, *A&AS*, 79, 329